Ultrafine MoO_2-Carbon Microstructures Enable Ultralong-Life Power-Type Sodium Ion Storage by Enhanced Pseudocapacitance

Changtai Zhao, Chang Yu, Mengdi Zhang, Huawei Huang, Shaofeng Li, Xiaotong Han, Zhibin Liu, Juan Yang, Wei Xiao, Jianneng Liang, Xueliang Sun,* and Jieshan Qiu**

The achievement of the superior rate capability and cycling stability is always the pursuit of sodium-ion batteries (SIBs). However, it is mainly restricted by the sluggish reaction kinetics and large volume change of SIBs during the discharge/charge process. This study reports a facile and scalable strategy to fabricate hierarchical architectures where TiO_2 nanotube clusters are coated with the composites of ultrafine MoO_2 nanoparticles embedded in carbon matrix (TiO_2@MoO_2-C), and demonstrates the superior electrochemical performance as the anode material for SIBs. The ultrafine MoO_2 nanoparticles and the unique nanorod structure of TiO_2@MoO_2-C help to decrease the Na^+ diffusion length and to accommodate the accompanying volume expansion. The good integration of MoO_2 nanoparticles into carbon matrix and the cable core role of TiO_2 nanotube clusters enable the rapid electron transfer during discharge/charge process. Benefiting from these structure merits, the as-made TiO_2@MoO_2-C can deliver an excellent cycling stability up to 10 000 cycles even at a high current density of 10 A g^{-1}. Additionally, it exhibits superior rate capacities of 110 and 76 mA h g^{-1} at high current densities of 10 and 20 A g^{-1}, respectively, which is mainly attributed to the high capacitance contribution.

1. Introduction

With the ever-growing demands for energy and the intense appeal for reducing carbon emissions, the innovation of energy storage devices has received worldwide concerns in the past decades.[1] Among numerous available candidates, lithium-ion batteries (LIBs) as a predominant power source have been successfully employed in portable electronic devices (PEDs) and electric vehicles (EVs).[2] However, the large-scale application of LIBs for storing sustainable energy is overwhelmed by the high cost and the scarcity of lithium resources. In this case, sodium-ion batteries (SIBs) are attracting more and more attention as one of the potential and promising alternatives to LIBs due to the similar work mechanism and the overwhelming advantages with regard to the low cost and abundance of sodium resources.[2b,3] Nevertheless, how to achieve high-rate capability and long cycle life in SIBs still remains a great challenge due to the sluggish reaction kinetics and large volume expansion rooted in larger Na ionic radius.[2c,4] As such, it is important and urgent to accelerate the solid-state ion diffusion and accommodate the accompanying volume change.

The incorporation of pseudocapacitive charge storage into SIBs is one of the effective and promising approaches to overcoming the sluggish kinetics and achieving the high-rate capability.[5] Pseudocapacitive charge storage is based on the faradic reaction that occurs on or near the surface of the electrode materials.[6] It has been demonstrated that the rational design of electrode materials with high pseudocapacitive charge storage can effectively integrate these advantages containing the high energy density of battery materials and the high power density of electrical double layer capacitor materials.[6] Up to date, many inorganic compounds with pseudocapacitive features including the intrinsic pseudocapacitive materials (RuO_2, MnO_2, and *T*-Nb_2O_5) and extrinsic pseudocapacitive materials (MoS_2, MoO_2, V_2O_5, TiO_2, and SnS, etc.) have been successfully applied in SIBs and made a great breakthrough in rate capability.[7] In addition, for the sake of high pseudocapacitive charge storage, it is essential to design and construct extrinsic pseudocapacitive materials with a tuned structure that is favorable for rapid mass transport and fast electron transfer. And some compounds with unique structure, such as mesoporous structure, ultrathin nanosheets, nanoparticles, nanowires, etc., have been successfully fabricated, leading to high pseudocapacitive charge storage and an excellent rate capability in SIBs.[7d,f,8] Nevertheless, the inferior cycling stability caused by large volume

C. Zhao, Prof. C. Yu, M. Zhang, H. Huang, S. Li, X. Han, Z. Liu, J. Yang, Prof. J. Qiu
State Key Lab of Fine Chemicals
Liaoning Key Lab for Energy Materials and Chemical Engineering
School of Chemical Engineering
Dalian University of Technology
Dalian 116024, China
E-mail: chang.yu@dlut.edu.cn; jqiu@dlut.edu.cn
C. Zhao, W. Xiao, J. Liang, Prof. X. Sun
Department of Mechanical and Materials Engineering
University of Western Ontario
London N6A 5B9, Canada
E-mail: xsun9@uwo.ca

DOI: 10.1002/aenm.201602880

expansion remains a bottleneck problem and severely inhibits the practical applications of SIBs.

The ultrafine nanoparticles (smaller than 5 nm) possess small particle size and high ratio of surface area to volume that can significantly facilitate the ion transport and accommodate the mechanical strain much better than that of the large particle materials during sodium ion insertion/extraction process.[3b,9] Moreover, constructing the electrode materials with hierarchical structure is also another effective strategy to decrease the solid-state ion diffusion distance and release the volume expansion.[10] Thus, integrating ultrafine nanoparticles into highly conductive carbon matrixes with a hierarchical structure may be a promising approach to simultaneously achieving the outstanding rate capability and long cycle life.

Here, we report a novel approach to the rational design of the hierarchical architecture in which TiO_2 nanotube clusters are coated with the composites of ultrafine MoO_2 nanoparticles embedded in carbon matrix (TiO_2@MoO_2-C). The unique rod-shaped core–shell nanoarchitecture and the ultrafine MoO_2 nanoparticle can not only obviously decrease the ion diffusion length but also effectively accommodate the volume expansion. And the carbon matrix serves as conductive framework and TiO_2 nanotube clusters acts as cable core, which synergistically ensure the rapid electron transfer even at a high discharge/charge current density. Bacause of this, the as-made TiO_2@MoO_2-C as the anode material for SIBs has exhibited an excellent electrochemical performance, evidenced by the ultralong cycle life up to 10 000 cycles at a high current density of 10 A g^{-1} and the excellent rate capability of 110 and 76 mA h g^{-1} at high current densities of 10 and 20 A g^{-1}, respectively.

2. Results and Discussion

Scheme 1 illustrates the typical synthesis process of TiO_2@MoO_2-C composites. Briefly, the TiO_2@MoO_2-C was synthesized via an in situ complexation and polymerization reactions of ammonium molybdate and dopamine in the presence of the TiO_2 nanotube templates, and followed by annealing. For comparison, the composites obtained by template-free polymerization (MoO_2-C) were also prepared following the same process in the absence of the TiO_2 nanotube templates.

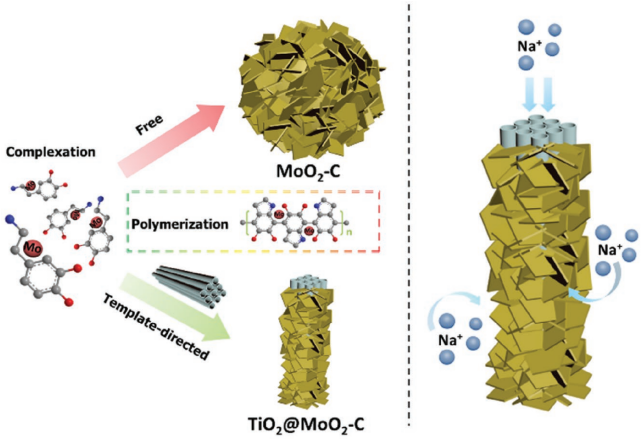

Scheme 1. Schematic illustration for the synthesis of the as-made TiO_2@MoO_2-C, and the Na^+ transfer behaviors within the TiO_2@MoO_2-C electrode matrix.

The morphologies and structure of the as-made samples were examined by scanning electron microscopy (SEM) and transmission electron microscopy (TEM), of which the representative images are shown in **Figure 1**. Figure 1a and Figures S1–S3 (Supporting Information) show that the MoO_2-C composites have a uniform sphere-shaped structure made of nanosheets, with a diameter of ≈500 nm. However, this is not the case for the TiO_2@MoO_2-C. It can be clearly seen from Figure 1b,c that the TiO_2@MoO_2-C composites feature a typical nanorod-shaped structure with a reduced diameter of ≈250 nm due to the template-guided effects of TiO_2 nanotube clusters, which is in favor of reducing the ion diffusion length during the discharge/charge process. Meanwhile, the TiO_2 nanotube clusters served as the role of cable core can facilitate the electron transfer throughout the overall composites, which is further confirmed by the electrochemical results discussed below. The MoO_2-C coating layer on TiO_2 nanotube clusters is assembled by the curved thin nanosheets, and shows a rough

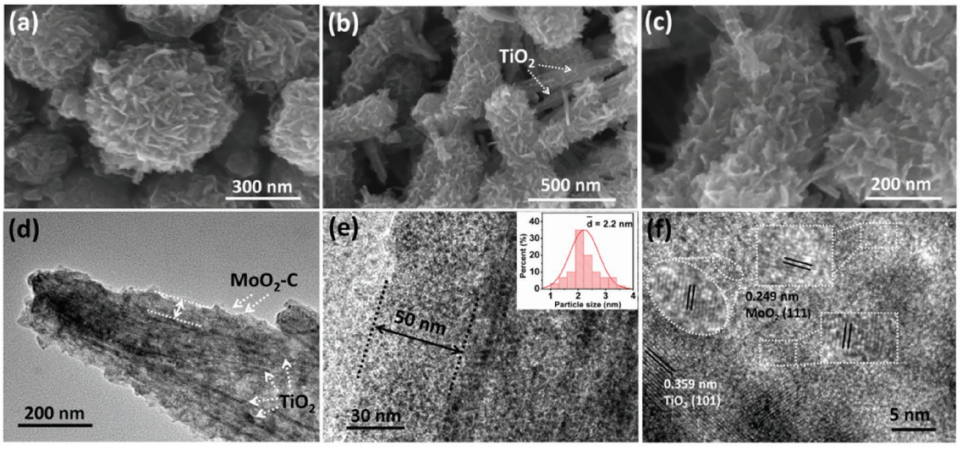

Figure 1. SEM images of a) MoO_2-C and b,c) TiO_2@MoO_2-C. d,e) TEM and f) HR-TEM images of the as-made TiO_2@MoO_2-C; the inset in panel (e) shows the size distribution of the MoO_2 particles in the TiO_2@MoO_2-C composites.

surface that helps to increase the effective and contactable area between electrolyte and electrode.

The more detailed microscopic structure of TiO_2@MoO_2-C was investigated by TEM, of which the results are shown in Figure 1d–f. The typical core–shell structure of TiO_2@MoO_2-C can be clearly observed. As shown in Figure 1d, the TiO_2 nanotube clusters as the cable core are uniformly coated with the MoO_2-C composites with a thickness of ≈50 nm, which is much smaller than the size of MoO_2-C nanospheres. Benefiting from this characteristic, the Na^+ diffusion length will be shortened, and the mass transport will also be accelerated during electrochemical reaction process.[11] The further magnified TEM image (Figure 1e) shows that the MoO_2 features ultrafine nanoparticles with an average size of ≈2.2 nm (inset in Figure 1e), which is vitally important for the high efficient utilization, especially for a surface-controlled pseudocapacitance reaction involved in the electrochemical process. And the ultrafine MoO_2 nanoparticles are embedded in the highly conductive carbon matrix, which can help to facilitate electron transfer and accommodate the volume expansion during discharge/charge process.[12] Figure 1f shows the high-resolution TEM (HR-TEM) image of TiO_2@MoO_2-C. It can be clearly noted that the well-resolved lattice spacing of 0.359 nm corresponds to the (101) crystal plane of TiO_2 phase. The particles show the spacing between adjacent fringes of 0.249 nm, which can be assigned to the (111) plane of MoO_2. The pore structure of the as-made TiO_2, MoO_2-C, and TiO_2@MoO_2-C samples was analyzed by nitrogen adsorption technique. As shown in Figure S4a (Supporting Information), all the samples show the type IV adsorption and desorption isotherms. Meanwhile, the TiO_2@ MoO_2-C features the highest Brunauer-Emmett-Teller (BET) specific surface area (130 m^2 g^{-1}) than that of MoO_2-C (121 m^2 g^{-1}) and TiO_2 (42 m^2 g^{-1}). The pore size distribution shown in Figure S4b (Supporting Information) reveals that the TiO_2@ MoO_2-C features relatively large pore size in comparison with the as-made MoO_2-C, which is beneficial for the electrolyte transport.

The composition and surface chemical states of the composites were analyzed by Raman, X-ray diffraction (XRD), X-ray photoelectron spectroscopy (XPS), and thermogravimetric analysis (Figure S5, Supporting Information). As shown in the Raman spectra (**Figure 2**a), the TiO_2@MoO_2-C exhibits two remarkable peaks at 1369 and 1596 cm^{-1} corresponding to the D-band and the G-band of carbon materials, respectively, and there are also typically characteristic peaks of TiO_2 and MoO_2.[13] Meanwhile, relatively weak MoO_3 characteristic peaks are present due to the oxidization of the external MoO_2 in air. Figure 2b shows the XRD patterns of the TiO_2 and TiO_2@ MoO_2-C. It is noted that the TiO_2@MoO_2-C reveals the typical diffraction peaks of TiO_2 and MoO_2. Besides, the MoO_3 diffraction peaks can be observed in the XRD pattern of TiO_2@ MoO_2-C, which is consistent with the Raman results.

XPS survey spectrum shows that the as-made TiO_2@MoO_2-C mainly consists of C, Mo, Ti, and O elements (Figure S6, Supporting Information). As shown in the high-resolution C 1s spectrum (Figure 2c), the peaks of the C 1s can be resolved into three components: the main peak centered at 284.6 eV corresponds to C—C, whereas the peaks at the 285.5 and 288.9 eV can be fitted to C—O and O—C=O, respectively. According to the high-resolution Ti 2p spectrum shown in Figure 2d, three characteristic peaks centered at 458.9, 464.7, and 472.3 eV can be attributed to the Ti $2p_{3/2}$, Ti $2p_{1/2}$ spin-orbit split peaks, and a satellite peak of Ti^{4+}, respectively. The energy separation between the $2p_{3/2}$ and $2p_{1/2}$ peaks is 5.8 eV, which is well consistent with that of TiO_2. From the surface high-resolution Mo 3d spectra (Figure 2e), it can be seen that the Mo mainly exists in the form of Mo^{4+} ($3d_{3/2}$, 233.0 eV) and Mo^{6+} ($3d_{3/2}$, 235.9 eV).[7c] To further investigate the electronic states inside the composites, the depth Mo 3d XPS spectra of TiO_2@ MoO_2-C are shown in Figure 2f, which were examined after different plasma etching time. Obviously, the peak intensity of Mo^{6+} decreases sharply with an increase of etching time, and inside the composite almost all is Mo^{4+} after 90 s etching, demonstrating that the Mo^{6+} only exists on the surface of TiO_2@ MoO_2-C, which may be attributed to the surface oxidation when

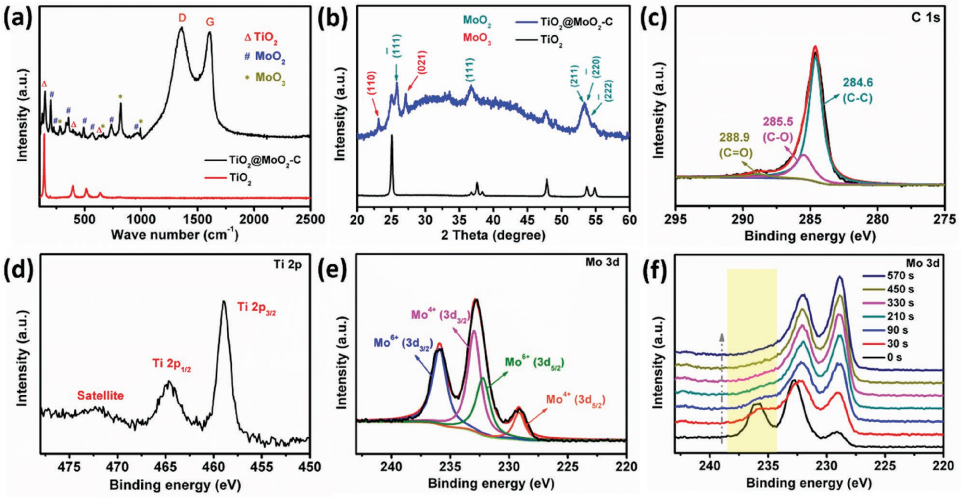

Figure 2. a) Raman spectra and b) XRD patterns of the as-made TiO_2 and TiO_2@MoO_2-C. c) C 1s and d) Ti 2p XPS spectra of TiO_2@MoO_2-C. e) Mo 3d XPS spectra of TiO_2@MoO_2-C without plasma etching. f) Mo 3d depth XPS spectra of TiO_2@MoO_2-C at different plasma etching time.

exposed into the air. This is also consistent with the results of XRD and Raman characterizations. All these results have shown that the TiO_2@MoO_2-C nanorods are successfully fabricated, in which the TiO_2 nanotube clusters serve as the core are coated with the composites of ultrafine MoO_2 nanoparticles embedded in carbon matrix. These integrated components and structure merits will be beneficial for electrochemical performances in SIBs.

The SIBs performances of the as-made TiO_2@MoO_2-C were tested using a 2032-type coin cells by galvanostatic discharge–charge and cyclic voltammetry (CV, Figure S7, Supporting Information) methods with a voltage window of 0.01–3.0 V. **Figure 3**a shows the first three galvanostatic discharge–charge profiles of the TiO_2@MoO_2-C at a current density of 50 mA g^{-1}. A high initial discharge specific capacity of 699 mA h g^{-1} is delivered, with a high reversible charge specific capacity of 297 mA h g^{-1} that is higher than that of the MoO_2-C (238 mA h g^{-1} of charge specific capacity, Figure S8b, Supporting Information) and TiO_2 (50 mA h g^{-1} of charge specific capacity, Figure S8a, Supporting Information). The large irreversible capacity in the first cycle mainly stems from the formation of the solid electrolyte interface layer on the electrode surface.[14] The cycle performance of the TiO_2@MoO_2-C was evaluated by galvanostatic discharge–charge measurement. As shown in Figure 3b, the TiO_2, MoO_2-C, and TiO_2@MoO_2-C electrodes all exhibit excellent cycling stability at a current density of 1 A g^{-1}, but TiO_2@MoO_2-C electrode achieves the most appreciable capacity. After 500 cycles, the TiO_2@MoO_2-C electrode shows a high reversible capacity of 210 mA h g^{-1}, which is higher than 146 mA h g^{-1} of MoO_2-C and 56 mA h g^{-1} of TiO_2. It is also higher than that of the N-doped carbon derived from polydopamine (NC, 49 mA h g^{-1} at 1 A g^{-1}) and the TiO_2@N-doped carbon (TiO_2@NC, 128 mA h g^{-1} at 1 A g^{-1}, Figure S9, Supporting Information). In order to evaluate the long-term and high-rate cycling stability, the TiO_2@MoO_2-C was further evaluated at high current densities of 5 and 10 A g^{-1} (Figure 3c). It is notable that the battery delivers an ultralong cycle life up to 10 000 cycles without obvious decay. Furthermore, the rate capability of the TiO_2@MoO_2-C was investigated by increasing the current densities from 0.05 to 20 A g^{-1} (Figure 3d). The high specific capacities of 110 and 76 mA h g^{-1} can be obtained even at large current densities of 10 and 20 A g^{-1}, respectively, which significantly outperform those of the MoO_2-C and TiO_2. Meanwhile, these high capacities correspond to ≈37.8 and 26.1% of the discharge capacity (291 mA h g^{-1}) at 0.05 A g^{-1} although the current densities increase 200-fold and 400-fold, respectively. In this case, the battery can achieve full discharge or charge in just 13.7 s, which is vitally important and promising for the fast-charging PEDs and EVs. In addition, when the current density is back to 0.05 A g^{-1} again, the reversible capacity can recover

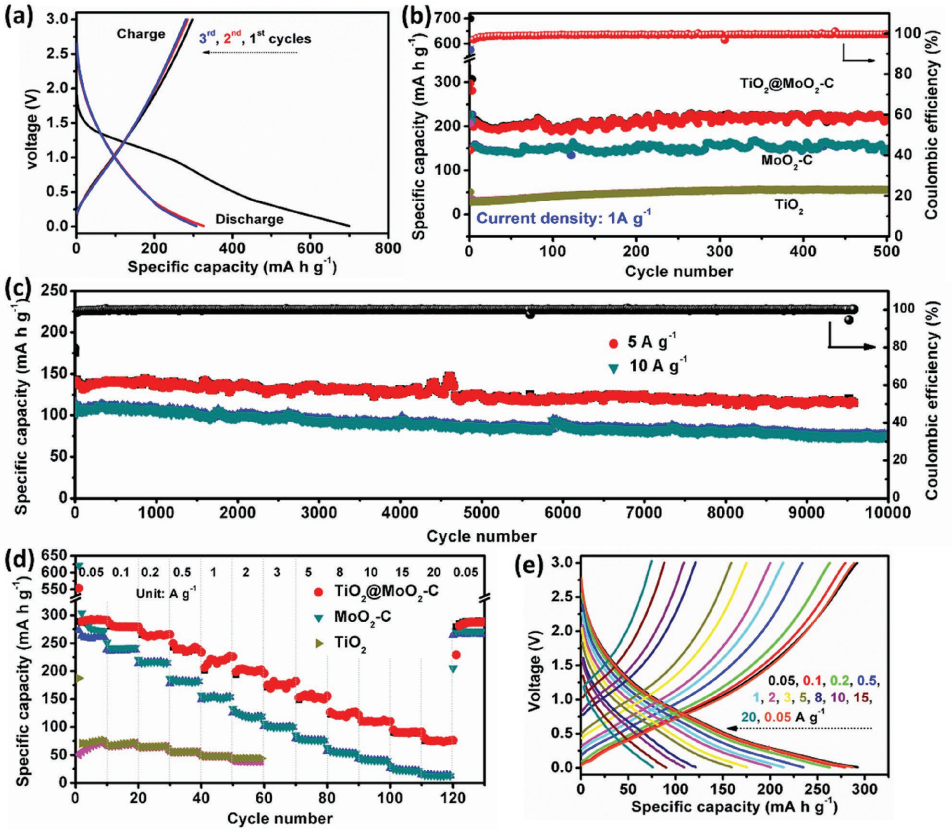

Figure 3. Electrochemical performances of the as-made TiO_2@MoO_2-C. a) The first three discharge–charge profiles of the TiO_2@MoO_2-C at a current density of 50 mA g^{-1}. b) The cycle performances of TiO_2, MoO_2-C, and TiO_2@MoO_2-C at a current density of 1 A g^{-1}. c) The cycle performance of TiO_2@MoO_2-C at current densities of 5 and 10 A g^{-1}. d) The rate performances of TiO_2, MoO_2-C, and TiO_2@MoO_2-C at different current densities. e) The discharge–charge profiles of TiO_2@MoO_2-C at different current densities.

to 286 mA h g^{-1} corresponding to the 98.3% of the initial value, indicative of the outstanding electrochemical reversibility. These results manifest that the TiO_2@MoO_2-C exhibits the excellent electrochemical performances in terms of both cycling stability and rate capability. **Figure 4** shows the comparisons of the rate performance and cycling stability of anode materials between the present work and previous work in the literature. It can be seen that the rate capability and cycling stability of the as-made TiO_2@MoO_2-C are comparable to the best performances reported in the literature.[15]

To further figure out the reason for the excellent rate performance of TiO_2@MoO_2-C, electrochemical impedance spectroscopy (EIS) was performed within the frequency range from 100 kHz to 0.01 Hz at open circuit potential. According to the Nyquist plots shown in **Figure 5**a, the TiO_2@MoO_2-C electrode shows a smaller diameter of the semicircle in the high-medium frequency region, indicative of a lower charge-transfer resistance (R_{ct}) and higher conductivity of TiO_2@MoO_2-C than that of MoO_2-C. This is due to the high conductivity of TiO_2, which is also confirmed by the lowest R_{ct} value (Figure 5a). Moreover, the TiO_2@MoO_2-C electrode shows a larger slope than that of MoO_2-C electrode in the low-frequency region of Nyquist plots, suggesting a small Warburg impedance that corresponds to a fast solid-state ion diffusion in the electrode bulk.[16] The superior electronic and ionic conductivity is attributed to the cable core role of TiO_2 nanotube clusters and the nanorod-shaped core–shell hierarchical structure of TiO_2@MoO_2-C. The pseudocapacitive nature of TiO_2@MoO_2-C can be demonstrated by the sloping discharge–charge profiles without distinct plateau

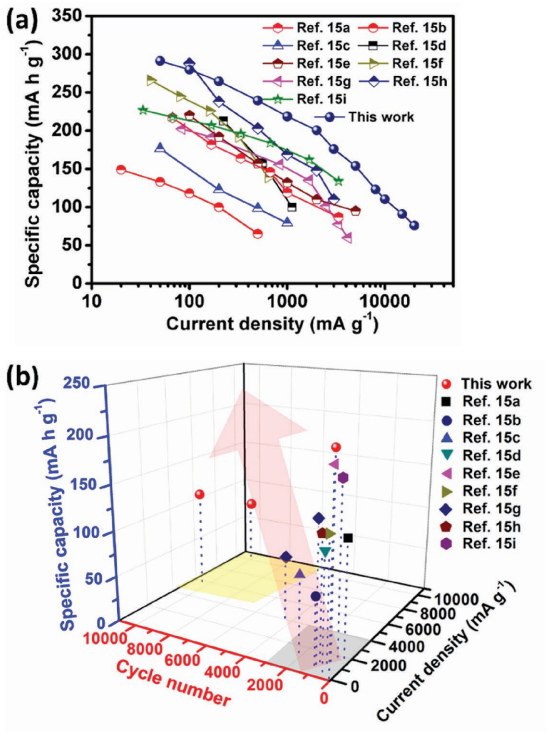

Figure 4. The comparison of a) the rate performance and b) cycling stability of anode materials in the present work and previous work in literature.

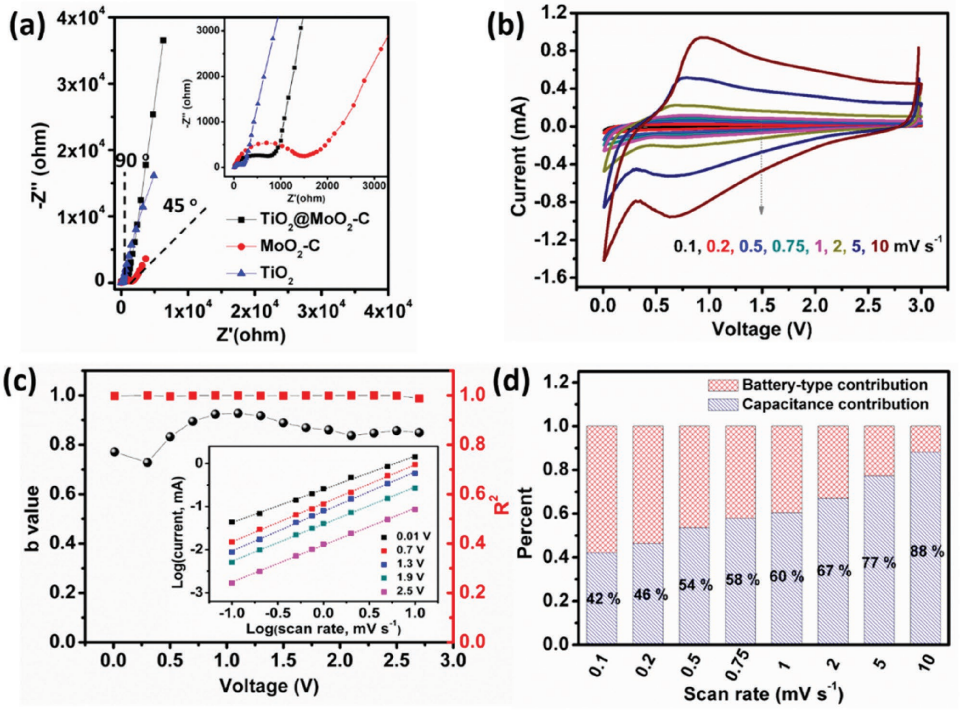

Figure 5. a) Nyquist plots of the TiO_2, MoO_2-C, and TiO_2@MoO_2-C electrodes tested at open circuit potential. b) CV curves of the TiO_2@MoO_2-C at different scan rates. c) *b* values plotted against battery voltage of the TiO_2@MoO_2-C for cathodic scans, the inset is the current response plotted against scan rates of TiO_2@MoO_2-C at different voltages. d) The percentage of capacitance contribution at different scan rates.

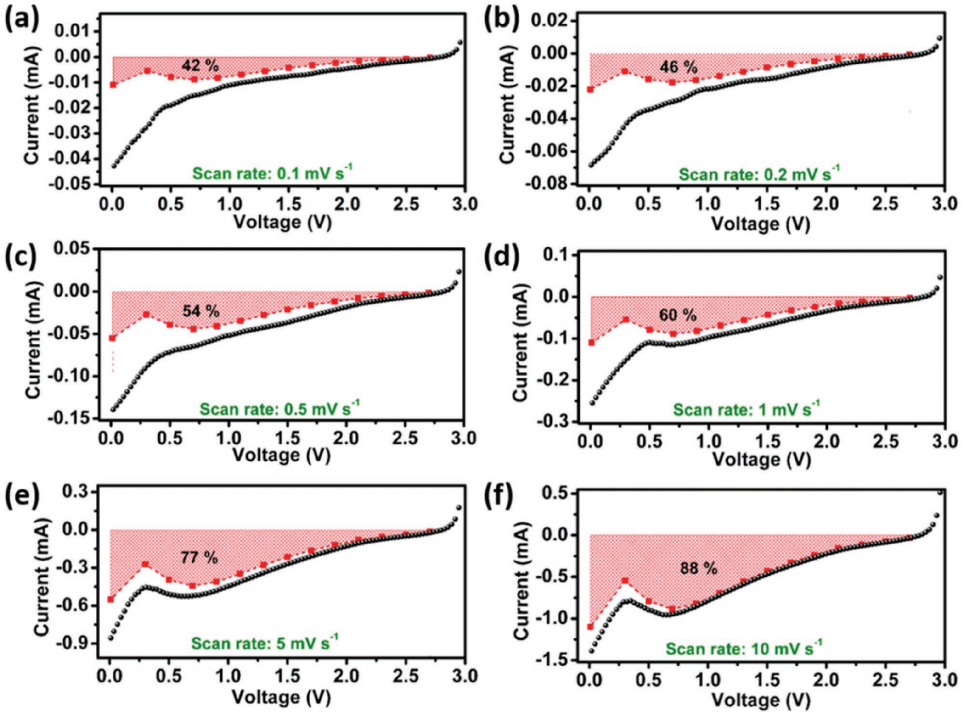

Figure 6. The capacitive contribution to charge storage of TiO_2@MoO_2-C at different scan rates of a) 0.1, b) 0.2, c) 0.5, d) 1, e) 5, and f) 10 mV s^{-1}.

regions at different current densities, which is a typical characteristic of pseudocapacitive materials (Figure 3e).[7d,8a]

To further have thorough insights into the pseudocapacitive contribution in the electrochemical performance, the CV tests of the TiO_2@MoO_2-C were carried out at various scan rates from 0.1 to 10 mV s^{-1}, of which the results are shown in Figure 5b. In this case, the current response at a particular voltage can be considered to contain capacitive contribution (k_1v) and diffusion-controlled contribution ($k_2v^{1/2}$). Also, it can be assumed that the current response obeys an exponential relationship with the scan rate[6,17]

$$i = k_1v + k_2v^{1/2} = av^b \quad (1)$$

Here, k_1, k_2, and a are constants, v is the scan rate. b is a value ranging from 0.5 (diffusion-controlled contribution) to 1 (capacitive contribution). As shown in Figure 5c, it exhibits a series of b values larger than 0.8, which represents a high capacitive contribution for the as-made TiO_2@MoO_2-C electrode.[7b,f] Through calculating the k_1 and k_2 values at different voltages (Figure S10, Supporting Information), the ratios of capacitive contribution can be quantitatively determined and the results are shown in Figure 5d and **Figure 6**.[6] It can be found that with the increase of scan rates, the capacitive contribution further increases. And a high ratio of 88.0% can be achieved at a scan rate of 10 mV s^{-1}, which is also higher than that of the MoO_2-C electrode (Figures S11 and S12, Supporting Information). The high capacitive contribution is ascribed to the short ion diffusion length and rapid electron transfer, which is also the reason for the high-rate capability of TiO_2@MoO_2-C electrode.

3. Conclusion

In summary, we reported a facile and scalable method for rational design and configuration of the nanorod-shaped core–shell architecture where TiO_2 nanotube clusters are coated with the composites of the ultrafine MoO_2 nanoparticles embedded in carbon matrix. The hierarchical structure of TiO_2@MoO_2-C and the ultrafine MoO_2 nanoparticles combines to effectively relieve the large volume change during discharge/charge process. Because of this, the TiO_2@MoO_2-C shows an excellent cycling stability up to 10 000 cycles. Furthermore, the core–shell structure of TiO_2@MoO_2-C and the ultrafine nanoparticles of MoO_2 help to decrease the ion diffusion length and facilitate the ion transport; meanwhile, the good integration of MoO_2 nanoparticles into the carbon matrix and the cable core role of TiO_2 nanotube clusters enable the rapid electron transfer. As a result, the as-made TiO_2@MoO_2-C electrode exhibits high capacitance and excellent rate capability. This work may help to inspire the configuration of advanced electrode materials for high-rate and long-life SIBs.

4. Experimental Section

Material Preparation: All reagents used in the present work were of analytical grade, and used without further purification.

Synthesis of the TiO_2 Nanotube Clusters Precursor: The TiO_2 nanotube clusters precursor were synthesized by a conventional method as reported in literature.[18] Typically, 0.4 g of P25 was dissolved into 60 mL of 10 M NaOH solution and then transferred to a Teflon-lined stainless steel autoclave of 80 mL, and held at 130 °C for 24 h with a strong magnetic stirring of 550 r min^{-1}. After cooling down, the product was washed with deionized water until pH ≈ 9. Finally, the obtained sample

was undergone a hydrogen ion exchange process in a diluted HNO_3 solution (0.1 M) and then washed for several times till pH ≈ 7. After that, the TiO_2 nanotube clusters precursor was dried for further use.

Synthesis of TiO_2@MoO_2-C, MoO_2-C, and TiO_2: 100 mg of TiO_2 nanotube clusters precursor was dispersed into 80 mL of deionized water under ultrasonic treatment for 15 min. Then 800 mg of $(NH_4)_6Mo_7O_{24}{\cdot}4H_2O$ and 200 mg of dopamine were dissolved into above dispersed solution. 160 mL of ethanol was added and followed by strong magnetic stirring for 5 min. After that, 1.2 mL of ammonia solution (28%–30%) was added, and the solution was subjected to continuous stirring for 1.5 h at room temperature. The precursor was obtained by centrifugation with ethanol for two times and vacuum drying at 50 °C for 10 h. Finally, the TiO_2@MoO_2-C composites were made by treating the precursor at 750 °C for 3 h at a ramping rate of 5 °C min^{-1} in flowing Ar atmosphere. For comparison, the MoO_2-C was fabricated in the absence of TiO_2 nanotube clusters precursor, and the TiO_2 was also prepared by annealing TiO_2 nanotube clusters precursor under the same conditions. The NC and TiO_2@NC were also prepared under the same conditions in the absence of Mo source and TiO_2, and Mo source, respectively.

Materials Characterization: The morphology, structure, and composition of the as-made samples were examined by SEM (Hitachi S-4800), TEM (FEI TF30), XRD (Bruker D8 Advance, Cu K α X-ray source), Raman (HORIBA Scientific LabRAM HR), and XPS (Thermo ESCALAB 250).

Electrochemical Measurements: The electrochemical performances of the as-made samples were evaluated by a 2032-type coin cell. The anode was prepared by casting the slurry containing 80 wt% of the as-made samples (TiO_2@MoO_2-C, MoO_2-C, and TiO_2), 10 wt% of polyvinylidene difluoride binder, and 10 wt% of carbon black in *N*-methyl-2-pyrrolidone solvent onto the Cu foil and then dried at 85 °C for 10 h. The assembly of the sodium-ion cell was carried out in an argon-filled glove box with a sodium foil, electrolyte (1 M $NaClO_4$ in ethylene carbonate and diethyl carbonate (volume ratio of 1:1) with 10 wt% of fluoroethylene carbonate additive), a glass fiber separator, and the as-made anodes. The galvanostatic discharge/charge tests were performed in an Arbin battery test station with a voltage window of 0.01–3.0 V at 25 °C. The CV and EIS tests were conducted on a Biologic electrochemical workstation. The average areal loading amount of active materials in the electrode was 0.7–0.8 mg cm^{-2}.

Supporting Information

Supporting Information is available from the Wiley Online Library or from the author.

Acknowledgements

This work was partly supported by the NSFC (Nos. 21522601, U1508201, and 21361162004), the Fundamental Research Funds for the Central Universities (DUT16ZD217), Natural Sciences and Engineering Research Council of Canada (NSERC), Canada Research Chair Program (CRC), Canada Foundation for Innovation (CFI), Ontario Research Fund (ORF), and the University of Western Ontario. C.Z. is supported by the Chinese Scholarship.

Received: December 23, 2016
Revised: January 23, 2017
Published online: April 21, 2017

[1] a) W. Deng, J. Qian, Y. Cao, X. Ai, H. Yang, *Small* **2016**, *12*, 583; b) Y.-X. Wang, J. Yang, S.-L. Chou, H. K. Liu, W.-x. Zhang, D. Zhao, S. X. Dou, *Nat. Commun.* **2015**, *6*, 8689; c) S.-W. Zhang, W. Lv, C. Luo, C.-H. You, J. Zhang, Z.-Z. Pan, F.-Y. Kang, Q.-H. Yang, *Energy Storage Mater.* **2016**, *3*, 18; d) S. Kajiyama, L. Szabova, K. Sodeyama, H. Iinuma, R. Morita, K. Gotoh, Y. Tateyama, M. Okubo, A. Yamada, *ACS Nano* **2016**, *10*, 3334.

[2] a) J. Wang, C. Luo, T. Gao, A. Langrock, A. C. Mignerey, C. Wang, *Small* **2015**, *11*, 473; b) N. Yabuuchi, K. Kubota, M. Dahbi, S. Komaba, *Chem. Rev.* **2014**, *114*, 11636; c) D. Xie, X. Xia, Y. Zhong, Y. Wang, D. Wang, X. Wang, J. Tu, *Adv. Energy Mater.* **2016**, *6*, 1601804; d) L. David, R. Bhandavat, G. Singh, *ACS Nano* **2014**, *8*, 1759.

[3] a) J. Sun, H.-W. Lee, M. Pasta, H. Yuan, G. Zheng, Y. Sun, Y. Li, Y. Cui, *Nat. Nanotechnol.* **2015**, *10*, 980; b) Y. Zheng, T. Zhou, C. Zhang, J. Mao, H. Liu, Z. Guo, *Angew. Chem. Int. Ed.* **2016**, *55*, 3408; c) D. Su, S. Dou, G. Wang, *Adv. Energy Mater.* **2015**, *5*, 1401205; d) D. Xu, C. Chen, J. Xie, B. Zhang, L. Miao, J. Cai, Y. Huang, L. Zhang, *Adv. Energy Mater.* **2016**, *6*, 1501929.

[4] a) Z. Hu, L. Wang, K. Zhang, J. Wang, F. Cheng, Z. Tao, J. Chen, *Angew. Chem. Int. Ed.* **2014**, *53*, 12794; b) T. Yang, T. Qian, M. Wang, X. Shen, N. Xu, Z. Sun, C. Yan, *Adv. Mater.* **2016**, *28*, 539; c) Y. Zhang, P. Zhu, L. Huang, J. Xie, S. Zhang, G. Cao, X. Zhao, *Adv. Funct. Mater.* **2015**, *25*, 481; d) S. Wang, L. Xia, L. Yu, L. Zhang, H. Wang, X. W. Lou, *Adv. Energy Mater.* **2016**, *6*, 1502217; e) Y. Li, Y.-S. Hu, M.-M. Titirici, L. Chen, X. Huang, *Adv. Energy Mater.* **2016**, *6*, 1600659.

[5] C. Chen, H. Xu, T. Zhou, Z. Guo, L. Chen, M. Yan, L. Mai, P. Hu, S. Cheng, Y. Huang, J. Xie, *Adv. Energy Mater.* **2016**, *6*, 1600322.

[6] a) J. Wang, J. Polleux, J. Lim, B. Dunn, *J. Phys. Chem. C* **2007**, *111*, 14925; b) V. Augustyn, P. Simon, B. Dunn, *Energy Environ. Sci.* **2014**, *7*, 1597.

[7] a) C. Chen, Y. Wen, X. Hu, X. Ji, M. Yan, L. Mai, P. Hu, B. Shan, Y. Huang, *Nat. Commun.* **2015**, *6*, 6929; b) D. Chao, C. Zhu, P. Yang, X. Xia, J. Liu, J. Wang, X. Fan, S. V. Savilov, J. Lin, H. J. Fan, Z. X. Shen, *Nat. Commun.* **2016**, *7*, 12122; c) H.-S. Kim, J. B. Cook, S. H. Tolbert, B. Dunn, *J. Electrochem. Soc.* **2015**, *162*, A5083; d) E. Lim, C. Jo, M. S. Kim, M.-H. Kim, J. Chun, H. Kim, J. Park, K. C. Roh, K. Kang, S. Yoon, J. Lee, *Adv. Funct. Mater.* **2016**, *26*, 3711; e) J. B. Cook, H.-S. Kim, Y. Yan, J. S. Ko, S. Robbennolt, B. Dunn, S. H. Tolbert, *Adv. Energy Mater.* **2016**, *6*, 1501937; f) Z. Chen, V. Augustyn, X. Jia, Q. Xiao, B. Dunn, Y. Lu, *ACS Nano* **2012**, *6*, 4319.

[8] a) X. Wang, S. Kajiyama, H. Iinuma, E. Hosono, S. Oro, I. Moriguchi, M. Okubo, A. Yamada, *Nat. Commun.* **2015**, *6*, 6544; b) T. Brezesinski, J. Wang, S. H. Tolbert, B. Dunn, *Nat. Mater.* **2010**, *9*, 146; c) G. A. Muller, J. B. Cook, H.-S. Kim, S. H. Tolbert, B. Dunn, *Nano Lett.* **2015**, *15*, 1911; d) K. Zhang, M. Park, L. Zhou, G.-H. Lee, W. Li, Y.-M. Kang, J. Chen, *Adv. Funct. Mater.* **2016**, *26*, 6728.

[9] a) X. Wang, Y. Liu, Y. Wang, L. Jiao, *Small* **2016**, *12*, 4865; b) Y. Liu, N. Zhang, L. Jiao, J. Chen, *Adv. Mater.* **2015**, *27*, 6702; c) H. Hou, C. E. Banks, M. Jing, Y. Zhang, X. Ji, *Adv. Mater.* **2015**, *27*, 7861.

[10] a) C. Zhang, X. Wang, Q. Liang, X. Liu, Q. Weng, J. Liu, Y. Yang, Z. Dai, K. Ding, Y. Bando, J. Tang, D. Golberg, *Nano Lett.* **2016**, *16*, 2054; b) Z. Liu, X.-Y. Yu, X. W. Lou, U. Paik, *Energy Environ. Sci.* **2016**, *9*, 2314; c) X. Wang, L. Fan, D. Gong, J. Zhu, Q. Zhang, B. Lu, *Adv. Funct. Mater.* **2016**, *26*, 1104; d) Y. Wang, D. Kong, W. Shi, B. Liu, G. J. Sim, Q. Ge, H. Y. Yang, *Adv. Energy Mater.* **2016**, *6*, 1601057.

[11] J. Wang, J. Liu, H. Yang, D. Chao, J. Yan, S. V. Savilov, J. Lin, Z. X. Shen, *Nano Energy* **2016**, *20*, 1.

[12] a) J.-K. Kim, Y. Kim, S. Park, H. Ko, Y. Kim, *Energy Environ. Sci.* **2016**, *9*, 1264; b) H. Gao, T. Zhou, Y. Zheng, Y. Liu, J. Chen, H. Liu, Z. Guo, *Adv. Energy Mater.* **2016**, *6*, 1601037.

[13] G. Qin, X. Zhang, C. Wang, *J. Mater. Chem. A* **2014**, *2*, 12449.

[14] a) Z.-T. Shi, W. Kang, J. Xu, L.-L. Sun, C. Wu, L. Wang, Y.-Q. Yu, D. Y. W. Yu, W. Zhang, C.-S. Lee, *Small* **2015**, *11*, 5667; b) D. Zhang, W. Sun, Y. Zhang, Y. Dou, Y. Jiang, S. X. Dou, *Adv. Funct. Mater.*

2016, *26*, 7479; c) F. Zhang, C. Xia, J. Zhu, B. Ahmed, H. Liang, D. B. Velusamy, U. Schwingenschlögl, H. N. Alshareef, *Adv. Energy Mater.* **2016**, 1601188.

[15] a) Y. Yeo, J.-W. Jung, K. Park, I.-D. Kim, *Sci. Rep.* **2015**, *5*, 13862; b) K. Zhu, S. Guo, J. Yi, S. Bai, Y. Wei, G. Chen, H. Zhou, *J. Mater. Chem. A* **2015**, *3*, 22012; c) Y. Li, D. Wang, Q. An, B. Ren, Y. Rong, Y. Yao, *J. Mater. Chem. A* **2016**, *4*, 5402; d) S. Hariharan, K. Saravanan, P. Balaya, *Electrochem. Commun.* **2013**, *31*, 5; e) Y. Xu, M. Zhou, L. Wen, C. Wang, H. Zhao, Y. Mi, L. Liang, Q. Fu, M. Wu, Y. Lei, *Chem. Mater.* **2015**, *27*, 4274; f) D. Su, S. Dou, G. Wang, *Chem. Mater.* **2015**, *27*, 6022; g) Y. Zhang, C. W. Foster, C. E. Banks, L. Shao, H. Hou, G. Zou, J. Chen, Z. Huang, X. Ji, *Adv. Mater.* **2016**, *28*, 9391; h) S. Dong, L. Shen, H. Li, G. Pang, H. Dou, X. Zhang, *Adv. Funct. Mater.* **2016**, *26*, 3703; i) M. N. Tahir, B. Oschmann, D. Buchholz, X. Dou, I. Lieberwirth, M. Panthöfer, W. Tremel, R. Zentel, S. Passerini, *Adv. Energy Mater.* **2016**, *6*, 1501489.

[16] a) C. Wu, Y. Jiang, P. Kopold, P. A. van Aken, J. Maier, Y. Yu, *Adv. Mater.* **2016**, *28*, 7276; b) L. Wang, X. Bi, S. Yang, *Adv. Mater.* **2016**, *28*, 7672; c) S. H. Choi, Y. N. Ko, J.-K. Lee, Y. C. Kang, *Adv. Funct. Mater.* **2015**, *25*, 1780; d) L. Fan, X. Li, B. Yan, J. Feng, D. Xiong, D. Li, L. Gu, Y. Wen, S. Lawes, X. Sun, *Adv. Energy Mater.* **2016**, *6*, 1502057.

[17] a) C. Wang, Y. Fang, Y. Xu, L. Liang, M. Zhou, H. Zhao, Y. Lei, *Adv. Funct. Mater.* **2016**, *26*, 1777; b) C. Chen, B. Zhang, L. Miao, M. Yan, L. Mai, Y. Huang, X. Hu, *J. Mater. Chem. A* **2016**, *4*, 8172.

[18] Y. Tang, Y. Zhang, J. Deng, J. Wei, H. L. Tam, B. K. Chandran, Z. Dong, Z. Chen, X. Chen, *Adv. Mater.* **2014**, *26*, 6111.